In situ tempering of martensite during laser powder bed fusion of Fe-0.45C steel

(article starts on next page)

In situ tempering of martensite during laser powder bed fusion of Fe-0.45C steel

William Hearn [a,*], Kristina Lindgren [b], Johan Persson [c], Eduard Hryha [a]

[a] *Department of Industrial and Materials Science, Chalmers University of Technology, SE 41296 Gothenburg, Sweden*
[b] *Department of Physics, Chalmers University of Technology, SE 41296 Gothenburg, Sweden*
[c] *Department of Mechanical Engineering Science, Lund University, SE 22100 Lund, Sweden*

ARTICLE INFO

ABSTRACT

During laser powder bed fusion (L-PBF), materials experience cyclic re-heating as new layers are deposited, inducing an in situ tempering effect. In this study, the effect of this phenomenon on the tempering of martensite during L-PBF was examined for Fe-0.45C steel. Detailed scanning electron microscopy, transmission electron microscopy, atom probe tomography, and hardness measurements indicated that martensite was initially in a quenched-like state after layer solidification, with carbon atoms segregating to dislocations and to martensite lath boundaries. Subsequent tempering of this quenched-like martensite was the result of two in situ phenomena: (i) micro-tempering within the heat affected zone and (ii) macro-tempering due to heat conduction and subsequent heat accumulation. Hardness measurements showed that although both influenced martensite tempering, micro-tempering had the most significant effect, as it reduced martensite hardness by up to ~380 HV. This reduction was due to the precipitation of nano-sized Fe_3C carbides at the previously carbon-enriched boundaries. Lastly, the magnitude of in situ tempering was found to be related to the energy input, where increasing the volumetric energy density from 60 to 190 J/mm^3 reduced martensite hardness by ~100 HV. These findings outline the stages of martensite tempering during L-PBF and indicate that the level of tempering can be adjusted by tailoring the processing parameters.

1. Introduction

Laser powder bed fusion (L-PBF) is an additive manufacturing technique that utilizes thermal energy from a laser source to produce metallic components directly from computer-aided designs. Given the small diameter of the laser source and the layer-by-layer approach of the process, complex components with relatively high dimensional accuracy can be produced. Despite these benefits, L-PBF continues to see restrained adoption as a production technique. One of the reasons for this is the limited understanding of the as-produced microstructure that forms during the complex thermal history of the process.

Initially, during L-PBF, material is rapidly heated above the melting temperature, before rapidly cooling to ambient temperature at cooling rates of 10^4 to 10^6 K/s [1,2]. This is then followed by cycles of re-heating as new material becomes deposited on top of or beside the previously deposited material. This re-heating induces an intrinsic heat treatment that progressively tempers the material in situ, where the peak temperature during tempering decreases as the distance from the deposited material increases [3–5]. This creates an as-produced microstructure that

is somewhat similar to a conventionally quenched and tempered material. However, it is difficult to apply the conventional understanding of quenching and tempering to L-PBF, as this in situ tempering occurs in a cyclical manner, over very short time scales, and at high temperatures [3–5]. It is also localized, meaning that different portions of the material will experience different tempering conditions.

Studies on the effect of this intrinsic heat treatment during laser additive manufacturing have been performed for Ti [6–8], Al [9,10], and Ni alloys [11], as well as for martensitic stainless steel [12] and maraging steel [13–15]. However, the effect of this intrinsic heat treatment remains unexplored for carbon steel, which is one of the most widely used alloy systems due to its favorable hardness, strength, ductility, and wear resistance at low material cost [16].

Traditionally, carbon steel undergoes quenching and tempering to achieve the desired properties. This is because in the quenched state, the material is too hard and brittle due to the formation of un-tempered martensite. This martensite forms during quenching, as there is insufficient time for the diffusion of carbon atoms within the cooling austenite. This causes them to become entrapped at the octahedral sites of the face-

---

* Corresponding author.
E-mail address: hearn@chalmers.se (W. Hearn).

Table 1

Chemical composition of the examined Fe-0.45C steel powder.

	C (wt.%)	Si (wt.%)	Mn (wt.%)
Fe-0.45C	0.45	0.18	0.08

centered cubic (FCC) lattice of austenite, inducing the transformation to the distorted body-centered tetragonal (BCT) lattice of martensite [17]. The application of subsequent tempering provides the necessary driving force for the re-distribution of entrapped carbon atoms, that helps to improve material toughness and ductility [17]. The potential to induce martensite tempering in situ may alleviate the need for post-processing of these alloys and help expand the production capability of L-PBF.

However, using carbon steel is not common in traditional laser-based production techniques (e.g., welding). This is because the formation of un-tempered martensite coupled with high residual stresses causes these alloys to be susceptible to cracking and have poor processability. Recent studies by the authors on plain carbon [18] and low-alloy steel [19] found that these alloys could be produced defect-free by L-PBF, even without preheating of the build plate. This indicates that the intrinsic heat treatment induces substantial tempering of martensite during L-PBF that reduces the crack susceptibility of the alloys. Despite these promising results, a systematic categorization of how martensite is tempered during L-PBF has yet to be presented, making it difficult to characterize what phenomena are inducing and controlling tempering during the process.

The aim of the current study is to describe the stages of martensite tempering during L-PBF of Fe-0.45C steel. Multiple techniques, including scanning electron microscopy (SEM), transmission electron microscopy (TEM), atom probe tomography (APT), micro-hardness and nano-hardness, were used to characterize the initial and tempered states of martensite using site-specific analysis. Additionally, specimens were produced at different processing parameters to evaluate the variation in martensite tempering. The obtained results help to describe the stages of martensite tempering during L-PBF and illustrate how the level of tempering is related to the processing parameters.

2. Experimental

Pre-alloyed gas atomized powder (supplied by Höganäs AB, Sweden) was used as the feedstock material. The composition of the feedstock powder is shown in Table 1. Particle size distribution was measured using laser diffraction with a Malvern Mastersizer 3000 (Malvern, UK). With this methodology, the following particle size distribution of the feedstock was obtained: $D_{10} = 23.1\,\mu m$, $D_{50} = 40.2\,\mu m$, and $D_{90} = 65.0\,\mu m$.

With the abovementioned powder feedstock, $5 \times 5 \times 5\,mm^3$ specimens were produced using an EOS M100 machine (EOS GmbH, Germany). This machine is equipped with an Yb-fiber laser that has a maximum laser power of 200 W and a beam diameter of ~40 μm. During the L-PBF process, no pre-heating of the build plate was used and an oxygen level of ~0.1% was maintained within the building chamber using Ar gas. Regarding the scanning strategy, a stripe scan pattern was used, along with a scan rotation angle of 67°. Additionally, no outer-skin or top-skin parameter was applied during exposure. The chosen processing parameters were based on the volumetric energy density (VED), which describes the energy input during L-PBF. The VED is a function of the scan speed (v), hatch spacing (h), layer thickness (t), and laser power (P):

$$VED = \frac{P}{v * h * t}$$

Using a set layer thickness of 20 μm, hatch spacing of 70 μm, and laser power of 110 W specimens were produced at VEDs of 60, 100, and 190 J/mm^3 by varying the scan speed.
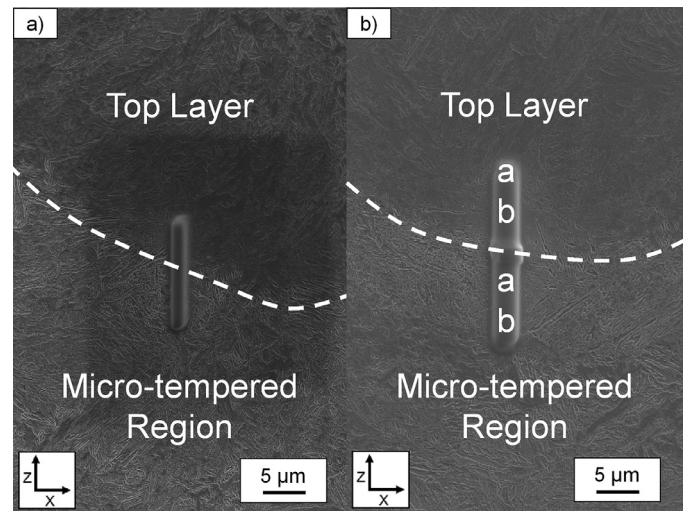

Fig. 1. Locations of lift-outs used for (a) TEM and (b) APT analyses, taken from an Fe-0.45C specimen produced at 100 J/mm^3. For APT, two site-specific specimens were taken from both the top layer and the micro-tempered regions. These specimens are referred to as "a" and "b," respectively. The boundary between the top layer and the micro-tempered region is highlighted using a white dashed line.

Analysis of the printed specimens involved the characterization of *XZ* cross sections, in which the *Z*-direction related to the building direction, whereas the *X*-direction related to the direction of gas flow. After sectioning, these cross sections were mounted and polished using a Struers TegraPol machine (Struers, Denmark). Then, after polishing, the specimens were etched with Nital (3%) to reveal the microstructure. The etched specimens were then imaged using a Zeiss AxioVision 7 light optical microscope (Carl Zeiss AG, Germany) and a Leo Gemini 1550 high-resolution SEM (Carl Zeiss AG, Germany).

Vickers micro-hardness tests were performed using a DuraScan 70 G5 machine (EMCO-TEST GmbH, Austria) and involved two sets of measurements. The first measurement set involved six HV10 indentations across the entire specimen in a 2×3 pattern, with each indentation spaced 2 and 1.5 mm apart, respectively. The second measurement set involved seven HV0.1 indentations along the *Z*-direction of the top layer, with each indentation spaced 0.04 mm apart.

Nano-hardness was measured using a NanoTest Vantage 4 machine (Micro Materials, UK). A load level of 20 mN was applied for each indentation, with loading and unloading times of 20 s. These nano-hardness measurements covered a total area of $150 \times 140\,\mu m$, with each indentation spaced 10 μm apart.

Both TEM and APT specimens were prepared by lift-out using a FEI Versa 3D focused ion beam SEM (Thermo Fisher Scientific, USA) to obtain site-specific specimens from both the top layer and the tempered regions below the top layer (see Fig. 1). TEM was performed in a FEI Tecnai T20 (Thermo Fisher Scientific, USA) with a LaB$_6$ filament operated at 200 kV. Moreover, APT analysis was performed in an Imago LEAP 3000X HR (Imago Scientific Instruments, USA) operated with a 0.3 nJ laser pulsing at 30 K. The target evaporation rate was set to 0.5%, and the pulse frequency was set to 200 kHz.

Reconstruction of the APT data was conducted using IVAS 3.6.14 software (CAMECA, France). An evaporation field of 23 V/nm and a *k*-value of 4.5 were assumed for the reconstructions. For the compositions provided in the text, the volumes were cut out with cylinders before evaluation. In addition, the C content was carefully evaluated as there were plenty of molecular ions containing C, including C, C$_2$, C$_3$, C$_4$, C$_5$, and FeC$_2$, both single- and double-charged. Special care was taken to deconvolute C$_2^+$ and C$_4^{2+}$ at m/n 24 Da, taking the minor C-13 isotopes at 25 and 24.5 Da into account.
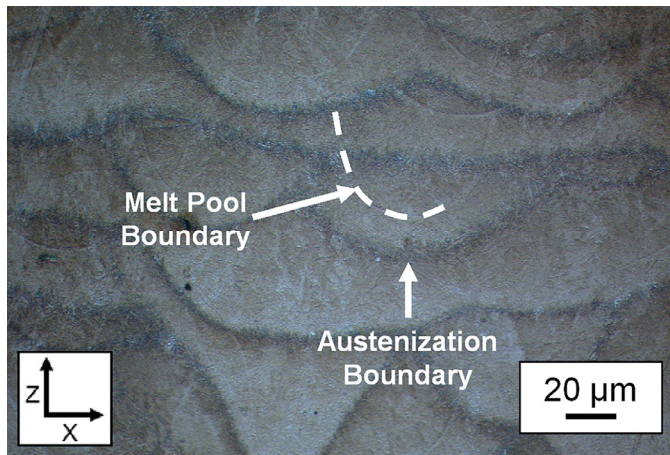
Fig. 2. Example of an austenization boundary (dark) and a melt pool boundary (diffuse) in a 100 J/mm³ specimen.
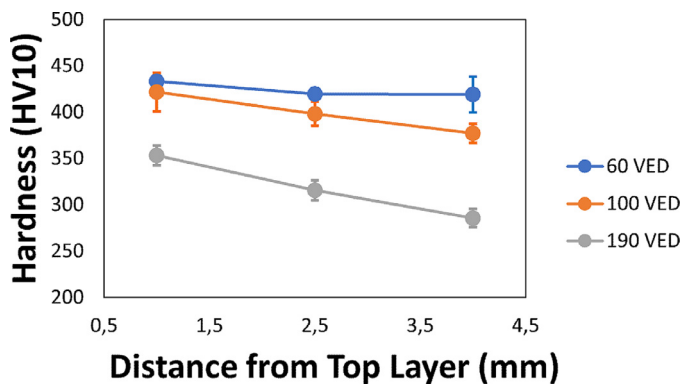

Fig. 3. Hardness depth profile for specimens produced at 60, 100, and 190 J/mm³.

3. Results

3.1. Optical microscopy and hardness

Optical microscopy (OM) revealed that the Fe-0.45C steel was primarily composed of tempered martensite (see Fig. 2). This observation was supported by hardness measurements (HV10), which revealed that the as-produced 60, 100, and 190 J/mm³ specimens exhibited bulk hardness values of 430 ± 16, 400 ± 22, and 330 ± 23 HV, respectively (see Fig. 3). These hardness values are similar to those of traditionally quenched and tempered Fe-0.45C steels [20]. OM also revealed preferentially etched bands within the tempered martensite (see Fig. 2). These dark bands related to the austenization boundaries, which indicate the portion of material heated above the austenite stability temperature during layer melting. The boundaries of the melt pool could also be ob-

served; however, they were fainter and etched as diffuse boundaries instead (see Fig. 2).

Small regions of un-tempered martensite were also observed and were predominantly located within the top layer of the specimens (see Fig. 4). These observations were supported by micro-hardness measurements (HV0.1), as martensite in this region exhibited a high hardness of approximately 750-800 HV. These hardness values are similar to those of traditionally quenched Fe-0.45C steels [20].

Variations in the VED did not affect the hardness of martensite within this top layer (see Fig. 5). However, it did affect the depth of the top layer, as increasing the VED increased the top layer depth from 87 ± 11 to 158 ± 15 to 263 ± 16 µm as the VED increased from 60 to 100 to 190 J/mm³, respectively. Additionally, increasing the VED decreased the martensite hardness of the tempered regions below the top layer (see Fig. 5).

Further nano-hardness measurements of the top layer and tempered regions below revealed a noticeable difference in properties between the two regions (see Table 2 and Fig. 6). As the martensite within the top layer exhibited a nano-hardness value of 6.8 ± 0.4 GPa, whereas the martensite within the tempered regions exhibited a value of 4.4 ± 0.2 GPa. The nano-hardness mapping also showed that the high hardness of martensite within the top layer was relatively uniform throughout this region (see Fig. 6).

3.2. Scanning electron microscopy

SEM analysis of the top layer revealed the presence of lath martensite (Fig. 7a) without any observable precipitates (see Fig. 7b). This un-tempered state was possible as this region of material did not experience re-heating during L-PBF, allowing it to maintain its as-deposited state. Regions of un-tempered martensite were also found within the specimen below lack of fusion pores, as these areas were preferentially revealed after Nital etching and exhibited a high hardness of ∼815 HV (see Fig. 8). The formation of un-tempered martensite below lack of fusion defects was possible as they blocked material tempering by inhibiting heat transfer between layers. Lastly, SEM analysis of the tempered regions below the top layer revealed a lath martensitic microstructure with an abundance of small precipitates (<100 nm in size; see Fig. 7c-d).

3.3. Transmission electron microscopy and atom probe tomography

Separate TEM and APT analyses were performed on Fe-0.45C specimens produced at 100 J/mm³ to examine the changes in martensite between the top layer and the tempered regions below. TEM of the top layer revealed a martensitic structure (see Fig. 9a) with no clear precipitates (see Fig. 9b). As for the tempered regions below, TEM analysis also revealed a martensitic structure (see Fig. 9c), but with an abundance of nano-sized precipitates (30–60 nm in size) throughout the martensite (see Fig. 9d).

Slices from the APT reconstructions of the top layer are shown in Fig. 10. In this region, carbon is unevenly distributed within the volume as it has segregated to specific microstructural features. Although APT
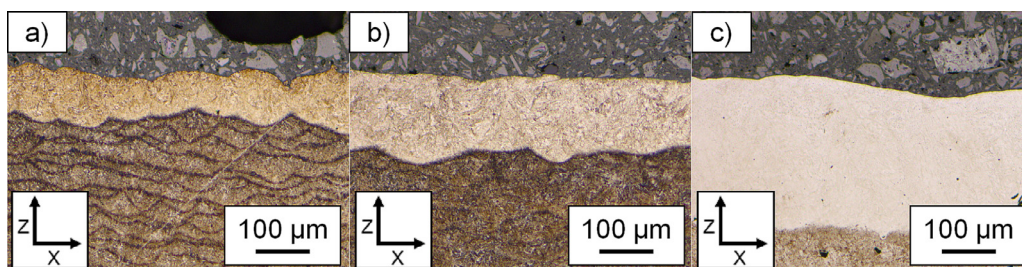

Fig. 4. Top layer containing un-tempered martensite in specimens produced at (a) 60, (b) 100, and (c) 190 J/mm³.

Table 2

Average nano-hardness taken from 30×30 μm areas within the top layer and within the tempered regions of a 100 J/mm^3 specimen.

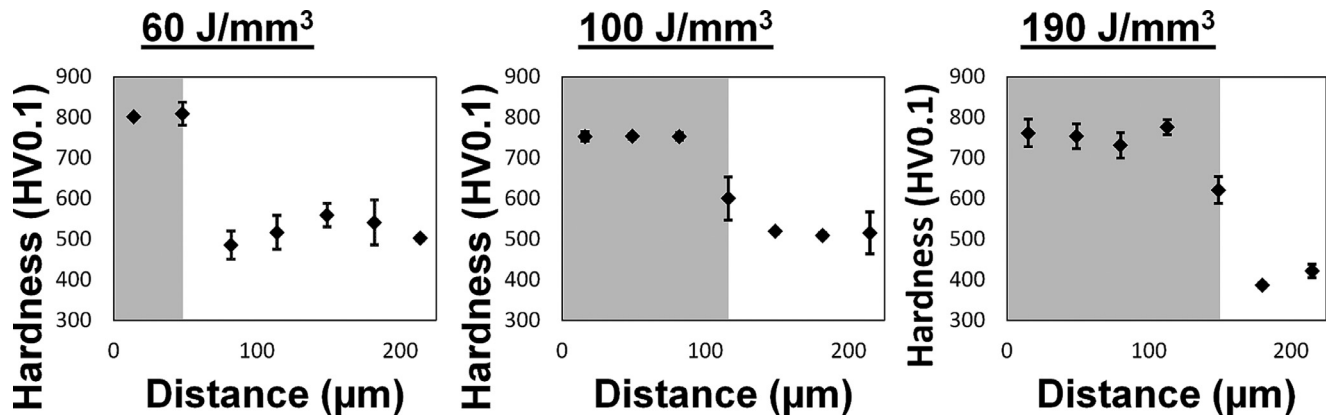|	Max. Depth (nm)	Plastic Depth (nm)	Max. Load (mN)	Hardness (GPa)	Er(GPa)
Top Layer	332 ± 9.4	295 ± 11.0	20	6.8 ± 0.4	201 ± 8.8
Tempered Region	405 ± 9.2	378 ± 10.3	20	4.4 ± 0.2	228 ± 14.6

Fig. 5. Micro-hardness (HV0.1) along the Z-direction, starting from the top layer in specimens produced at 60, 100, and 190 J/mm^3. The indentations taken within the top layer are indicated by a gray region.
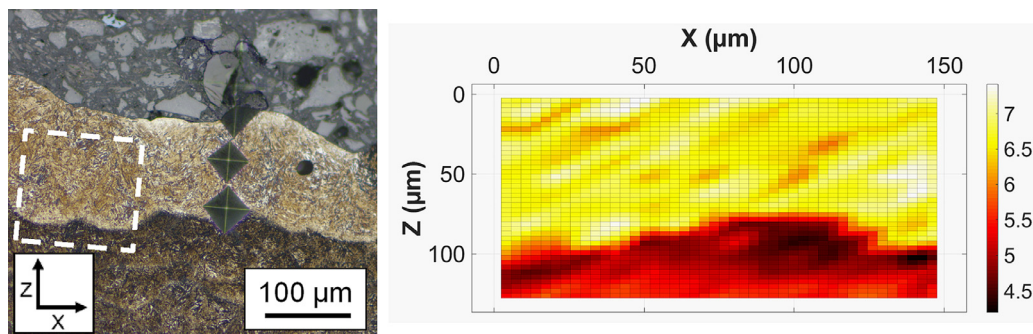

Fig. 6. Nano-hardness mapping (right) of indentations performed within the highlighted region (left) of a 100 J/mm^3 specimen. The range of nano-hardness was from 4 to 7.5 GPa.
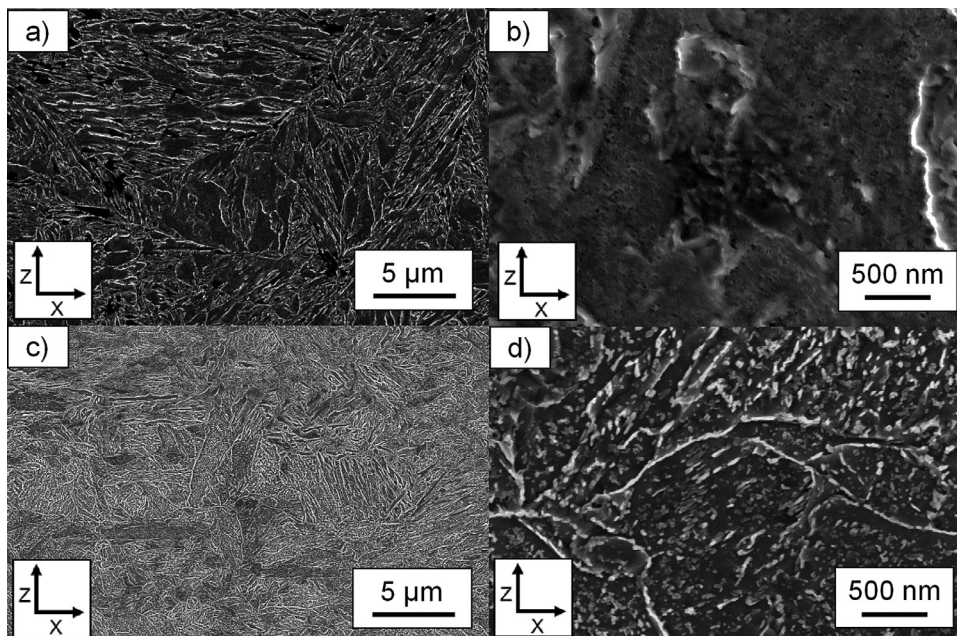

Fig. 7. (a) SEM image of un-tempered martensite found within the top layer of a 60 J/mm^3 specimen. (b) Higher magnification of (a) showing no noticeable precipitates. (c) SEM image of martensite found within the tempered region of a 100 J/mm^3 specimen. (d) Higher magnification of (c) revealing the presence of nano-sized (<100 nm) precipitates.
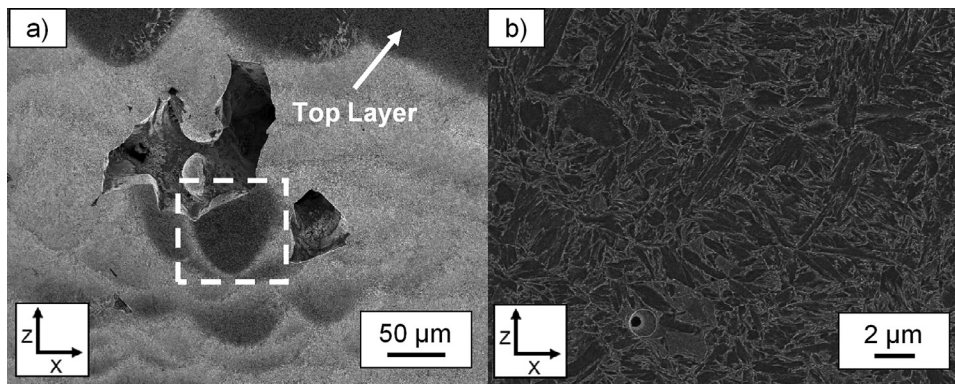
Fig. 8. (a) Area of un-tempered martensite (dashed box) found below a lack of fusion pore in a 60 J/mm³ specimen. (b) Higher-magnification image of un-tempered martensite from the boxed region in (a).
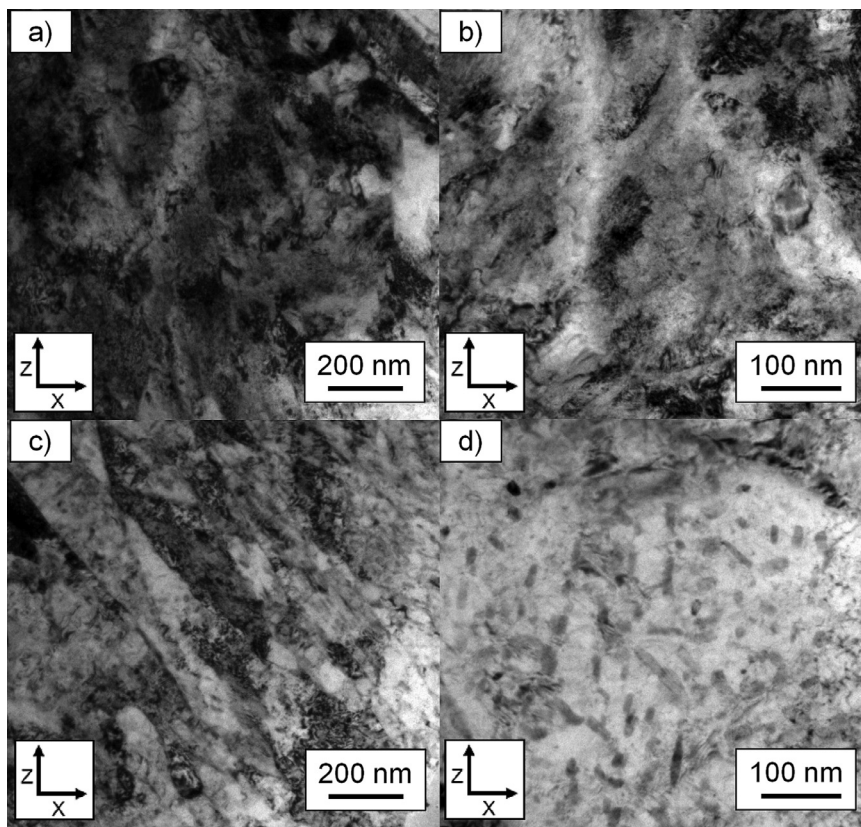

Fig. 9. (a) TEM image of the martensite found within the top layer of a 100 J/mm³ specimen. (b) Higher-magnification imaging of this region was unable to detect any precipitation. (c) TEM image of the martensite found within the tempered regions below the top layer of a 100 J/mm³ specimen. (d) Higher-magnification imaging of this region revealed numerous disc-shaped precipitates (30–60 nm in size).

Table 3

Composition from APT of the metal matrix volume and the high C volume (marked iii) in Fig. 9b within the top layer. Carbon-enriched dislocations and boundaries are not included in the composition determination of these volumes.

	Fe	C	Si	Al	Mn	V	Cr	Co	Ni	Cu
Metal Matrix Volume (at.%)	Bal.	0.44	0.21	0.00	0.12	0.08	0.02	0.02	0.03	0.01
High C Volume (at.%)	Bal.	2.14	0.17	0.14	0.09	0.06	0.03	0.01	0.01	0.01

does not provide crystallographic data, the distribution of carbon suggests likely segregation to dislocations (marked i) and lath boundaries (marked ii) at concentrations of up to 5–6 at.%. Between these features, the metal matrix contains a small amount of carbon (~0.44 at.%; see the full composition in Table 3), indicating that only a limited amount of carbon remains in solid solution. Fig. 10b shows a volume with a higher carbon content (marked iii). In this volume, the carbon content is 2.1 at.% (see Table 3 for the full composition), and is thus interpreted as retained austenite. Due to the small volume of APT analysis, the full size

and total volume fraction of austenite was not possible to determine. The edge of this retained austenite was enriched with carbon, similar to the lath boundaries. The blue precipitate shown in Fig. 10a is an Al-rich oxide, which also contains some Mn, Si, Cr, Fe, C, and Ti.

Slices from the APT reconstructions of the tempered region below the top layer are shown in Fig. 11. Unlike the top layer, the distribution of carbon atoms is different in these volumes as small, oblate carbides (marked i) are found sitting on carbon-enriched boundaries (marked ii). Some of the boundaries appear diffuse, due to cutting the slice shown in

Table 4

Average composition from APT of the metal matrix within the tempered region. Carbon-enriched dislocations and boundaries are not included in the composition determination of this volume.

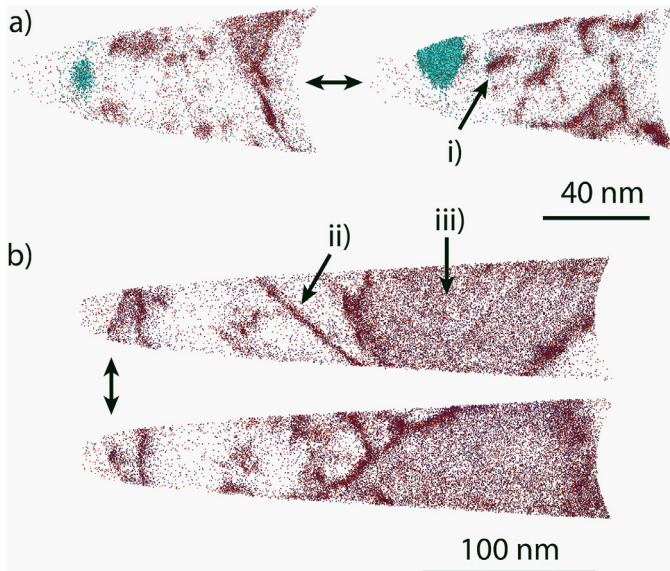|	Fe	C	Si	Al	Mn	V	Cr	Co	Ni	Cu
Metal Matrix Volume (at.%)	Bal.	0.16	0.17	0.00	0.09	0.06	0.02	0.01	0.01	0.01

Fig. 10. Slices of the APT reconstructions from the top layer. C, C_2, C_3, and C_4 ions are shown. Two 10 nm slices are shown for each analysis, with 90° in between. (a) also exhibits an Al-rich oxide inclusion, shown in blue. The marked features are (i) a carbon-decorated dislocation, (ii) a carbon-decorated boundary, and (iii) a region that is presumably retained austenite.
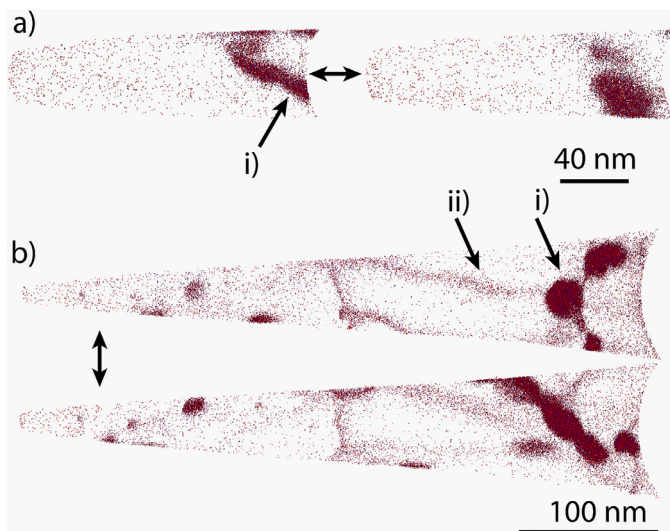

Fig. 11. Slices of APT reconstructions of the tempered regions directly below the top layer. C, C_2, C_3, and C_4 ions are shown. Two 10 nm thick slices are shown for each analysis, with a 90° rotation between the two. Carbides within the volumes are marked as i, and C-enriched boundary layers are marked as ii.

the Fig. with an angle. Both analyses in Fig. 11 show a slight decrease in the carbon content of the metal matrix (~0.16 at.%) when compared to that of the un-tempered top layer (~0.44 at.%). The full average composition of the volumes not containing carbon-rich layers is shown in Table 4.

The carbides within the tempered regions were approximately 30–60 nm in diameter and 10–20 nm in thickness. To determine their composition, they were separately analyzed and defined by iso-concentration surfaces. However, because of the small thickness of the carbides, along with the fact that the carbide–metal interface was somewhat diffuse (as a result of the APT analysis), the limit of the iso-concentration surfaces was found to significantly affect the carbide carbon content. Thus, the carbon content limit was set as high as possible to exclude any contribution from the metal matrix while still ensuring that the surfaces are reasonably smooth and that random fluctuations of a lower carbon content within the carbide bulk are not excluded. After careful peak deconvolution, the carbon content of the carbides was found to be 24.6 at.%. This is in line with the expected composition of cementite (Fe_3C, 25 at.%), which should be the same when analyzed by APT [21]. Additional examination of the carbides revealed that although the conducted APT analysis was laser-pulsed (making Si subject to surface diffusion prior to evaporation), there was noticeable rejection of Si toward the carbide interface and a corresponding depletion of Si within the carbide (see Fig. 12).

4. Discussion

To understand the in situ tempering of martensite during L-PBF, the initial un-tempered state needed to characterized first. This un-tempered martensite forms during layer melting for all material heated above the austenite stability temperature (T_A), as this region will transform into austenite before subsequently transforming into martensite upon cooling (see Fig. 13a). Analysis revealed that this un-tempered martensite had a high hardness (750-800 HV) and contained no carbides, in-line with the expected characteristics of quenched martensite. However, the carbon atoms were not distributed in true solid solution and were instead segregated at dislocations and martensite lath boundaries. This segregation is likely caused by the reduced solubility of carbon atoms within the octahedral sites of the martensite lattice, in addition to the high mobility of carbon atoms that can allow for some segregation to occur even during rapid cooling [17]. This segregation relates to a phenomenon known as auto-tempering which is commonly observed in traditionally quenched carbon steel [22,23]. Additionally, despite the lack of carbon atoms in solid solution, the segregated carbon will still provide a similar strengthening effect [22]. These findings indicate that un-tempered martensite in L-PBF is in a quenched-like state, where there is noticeable segregation of carbon atoms to dislocations and to martensite lath boundaries.

In the absence of build plate pre-heating, in situ tempering during L-PBF is the result of two phenomena. The first is micro-tempering, which is a rapid form of tempering that occurs within the heat affected zone during layer melting (see Fig. 13a). While the second is macro-tempering, which is related to heat conduction and subsequent heat accumulation within the solidified material that provides consistent tempering throughout the process (see Fig. 13b). Macro-tempering occurs as solidified material has a thermal conductivity approximately 100 times larger than the surrounding powder bed [24]. This induces conductive heat flow toward the build plate, as well as subsequent heat accumulation. This heat accumulation was detected by Chiumenti et al. [25], who found that the solidified material reached up to ~150°C above the ambient temperature and remained so in a quasi-steady state until the end of the L-PBF process.
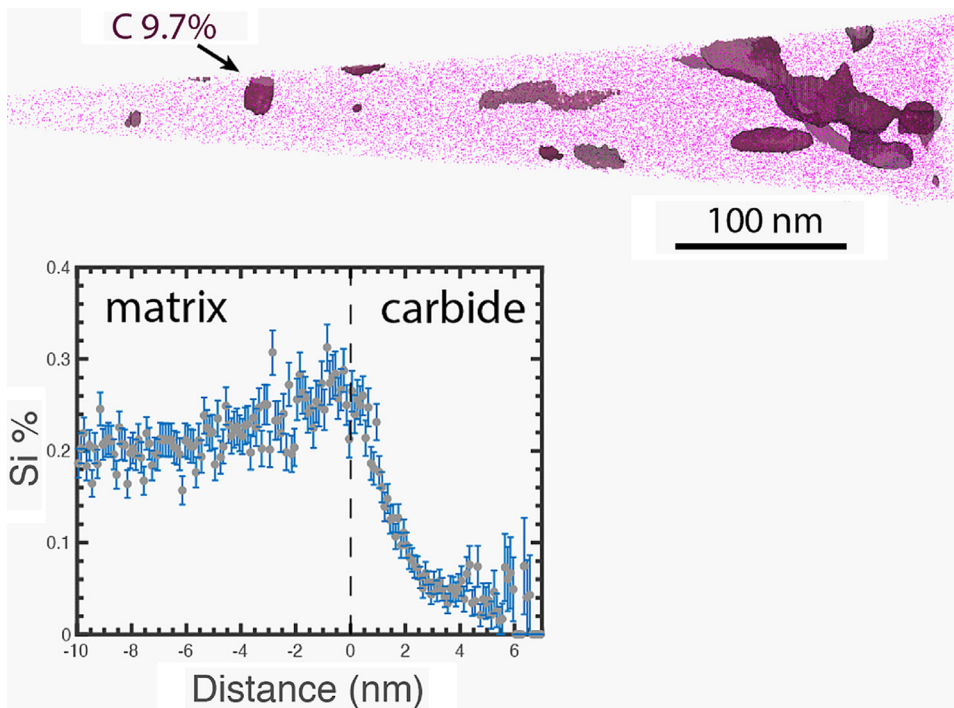
Fig. 12. Proxigram showing the Si distribution in relation to the 9.7% C iso-concentration surfaces outlining the carbides (burgundy). The pink dots show the outline of the atom probe reconstruction.
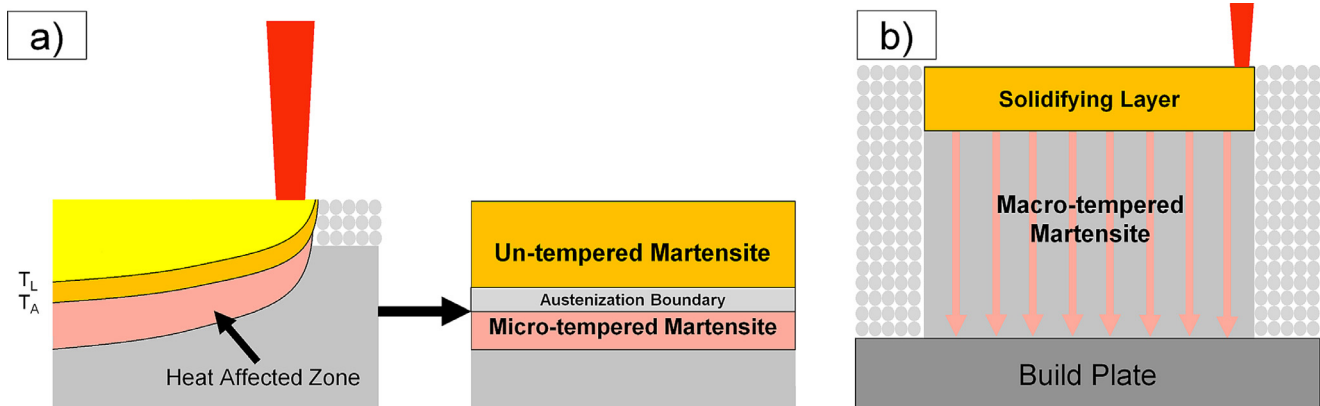

Fig. 13. (a) Schematic outlining the formation of un-tempered and micro-tempered martensite during layer melting. The material heated above the liquidus temperature (yellow) forms the melt pool, while the material heated above the austenite stability temperature (orange) forms un-tempered martensite and the material heated below the austenite stability temperature (pink) forms micro-tempered martensite. The distinction between the un-tempered and micro-tempered martensite is defined by the austenization boundary (grey). (b) Schematic outlining macro-tempering due to heat conduction and subsequent heat accumulation within the previously solidified material.

To compare the impact of both phenomena, extensive hardness measurements were performed. The results showed that although both forms of in situ tempering affected the specimen hardness, the reduction in hardness between the top layer and the micro-tempered regions reached ~380 HV according to micro-hardness measurements and ~2.4 GPa according to nano-hardness measurements. On the other hand, when comparing the hardness near the top versus the bottom specimen cross sections, the reduction in martensite hardness due to macro-tempering reached up to only ~67 HV. Moreover, martensite in the specimen that did not experience micro-tempering (e.g., areas below lack of fusion porosity) remained in an un-tempered state. These findings highlight that the greatest degree of martensite tempering occurs during micro-tempering.

The reduction in hardness from the un-tempered to micro-tempered martensite was due to change in carbon atom distribution, as carbon went from being segregated at boundaries and dislocations to forming a distributed network of nano-sized carbides. These carbides formed at the previously carbon enriched boundaries of un-tempered martensite, indicating that the initial segregation of carbon acted as a precursor to carbide nucleation. Further APT revealed that these carbides had a carbon content of 24.6 at.%, in line with the anticipated composition of cementite (Fe_3C). Additional proxigrams revealed the noticeable depletion of Si within the carbides, as well as a buildup of Si at the carbide–matrix interface. Typically, this rejection of Si occurs only during the later stages of cementite growth, following prolonged tempering times (>1 h) or increased tempering temperatures (>300°C) [26–28]. This is because during the early stages of tempering, cementite growth is controlled by the diffusion of carbon rather than the diffusion of substitutional elements like Si [26,29,30]. These findings indicate that micro-tempering induces the precipitation of nano-sized cementite at previously carbon-enriched boundaries, which noticeably reduces the hardness of martensite.

Lastly, the degree of martensite tempering during L-PBF was dependent upon the VED, as increasing from 60 to 190 J/mm³ decreased martensite hardness by ~100 HV within the micro- and macro-tempered

regions. This reduction was due to the increase in melt pool depth, which increased by approximately three times as the VED increased from 60 to 190 J/mm^3. These larger melt pools helped lower the thermal gradient and rate of heat transport during the solidification process [31], enhancing the level of the in situ tempering. The noticeable variation in martensite hardness with increasing VED indicates that the level of tempering during L-PBF can be adjusted by tailoring the processing parameters. Still, it is surprising to what extent said tempering can be adjusted, as the reduction in hardness from 60 to 190 J/mm^3 was equivalent to increasing the tempering temperature by ~100°C [20]. This noticeable improvement in tempering with increasing energy input is what can enable the crack-free processing of non-weldable carbon steel when using L-PBF.

5. Conclusions

This study focused on the in situ tempering of martensite during L-PBF of Fe-0.45C steel. The analysis showed that martensite is initially in a quenched-like state after layer solidification, with carbon atoms segregating to dislocations and to martensite lath boundaries. Subsequent tempering of this quenched-like martensite was the result of two in situ phenomena: (i) micro-tempering within the heat affected zone during layer melting and (ii) macro-tempering due to heat conduction and subsequent heat accumulation within the previously solidified material.

Although both phenomena affected the level of martensite tempering, hardness measurements showed that micro-tempering had the most significant effect, as it reduced martensite hardness by up to ~380 HV from micro-hardness measurements and by up to ~2.4 GPa from nano-hardness measurements. It was also found that martensite that did not experience micro-tempering (e.g., areas below lack of fusion porosity) would maintain in an un-tempered state, even within the specimen bulk.

This reduction in martensite hardness during micro-tempering was due to the precipitation of nano-sized carbides (30–60 nm) at the previously carbon-enriched boundaries. APT analysis revealed that the composition of the carbides was 24.6 at.% C and that there was noticeable rejection of Si. Both results strongly suggest that the observed carbides relate to cementite (Fe$_3$C).

Lastly, the level of martensite tempering during L-PBF was dependent upon the VED, where increasing the VED by 130 J/mm^3 reduced the hardness of martensite by ~100 HV. This reduction was related to the larger volume of re-heated material, which enhanced the level of in situ tempering. This indicates that the level of martensite tempering during L-PBF can be controlled by adjusting the processing parameters.

Declaration of Competing Interest

The authors declare that they have no known competing financial interests or personal relationships that could have appeared to influence the work reported in this paper.

Acknowledgment

Supplementary materials

Supplementary material associated with this article can be found, in the online version, at doi:10.1016/j.mtla.2022.101459.

References

[1] U. Bertoli, G. Guss, S. Wu, M. Matthews, J. Schoenung, In-situ characterization of laser-powder interaction and cooling rates through high-speed imaging of powder bed fusion additive manufacturing, Mater. Des. (135) (2017) 385–396.

[2] Y. Li, D. Gu, Parametric analysis of thermal behavior during selective laser melting additive manufacturing of aluminum alloy powder, Mater. Des. (63) (2014) 856–867.

[3] J. Zhang, Y. Liu, M. Bayat, Q. Tan, Y. Yin, Z. Fan, S. Liu, J. Hattel, M. Dargusch, M.-X. Zhang, Achieving high ductility in a selectively laser melted commercial pure-titanium via in-situ grain refinement, Scr. Mater. 191 (2021) 155–160.

[4] H. Chae, E.-W. Huang, W. Woo, S. Kang, J. Jain, K. An, S. Lee, Unravelling thermal history during additive manufacturing of martensitic stainless steel, J. Alloys Compd. 857 (2021).

[5] P. Promoppatum, S.-C. Yao, P. Pistorius, A. Rollett, P. Coutts, F. Lia, R. Martukanitz, Numerical modeling and experimental validation of thermal history and microstructure for additive manufacturing of an Inconel 718 product, Progress in Additive Manufacturing 3 (2018) 15–32.

[6] J. Yang, H. Yu, J. Yin, M. Gao, Z. Wang, X. Zeng, Formation and control of martensite in Ti-6Al-4V alloy produced by selective laser melting, Mater. Des. 108 (2016) 308–318.

[7] W. Xu, E. Lui, A. Pateras, M. Qian, M. Brandt, In situ tailoring microstructure in additively manufactured Ti-6Al-4V for superior mechanical performance, Acta Mater. 125 (2017) 390–400.

[8] P. Barriobero-Vila, J. Gussone, J. Haubrich, S. Sandlöbes, P. Da Silva, P. Cloetens, N. Schell, G. Requena, nducing Stable $\alpha + \beta$ Microstructures during Selective Laser Melting of Ti-6Al-4V Using Intensified Intrinsic Heat Treatments, Materials 10 (3) (2017).

[9] P. Kurnsteiner, P. Bajaj, A. Gupta, M. Wilms, A. Weisheit, X. Li, C. Leinenbach, B. Gault, E. Jagle, D. Raabe, Control of thermally stable core-shell nano-precipitates in additively manufacturing Al-Sc-Zr alloys, Additive Manufacturing 32 (2020).

[10] A. Spierings, K. Dawson, P. Uggowitzer, K. Wegener, Influence of SLM scan-speed on microstructure, precipitation of Al3Sc particles and mechanical properties in Sc- and Zr-modified Al-Mg alloys, Mater. Des. 140 (2018) 134–143.

[11] E. Jagle, Z. Sheng, L. Wu, L. Lu, J. Risse, A. Weisheit, D. Raabe, Precipitation Reactions in Age-Hardenable Alloys During Laser Additive Manufacturing, JOM 68 (3) (2016) 943–949.

[12] P.Y.I. Krakhmalev, G. Fredriksson, I. Yadroitsev, In situ heat treatment in selective laser melted martensitic 420 stainless steel, Mater. Des. 87 (2015) 380–385.

[13] E. Jägle, Z. Sheng, P. Kurnsteiner, S. Ocylok, A. Weisheit, D. Raabe, Comparison of Maraging Steel Micro- and Nanostructure Produced Conventionally and by Laser Additive Manufacturing, Materials 8 (10) (2017).

[14] P. Kurnsteiner, M. Wilms, A. Weisheit, P. Barriobero-Vila, E. Jagle, D. Raabe, Massive nanoprecipitation in an Fe-19Ni-xAl maraging steel triggered by the intrinsic heat treatment during laser metal deposition, Acta Mater. (129) (2017) 52–60.

[15] P. Kurnsteiner, M. Wilms, A. Weisheit, B. Gault, E. Jagle, D. Raabe, High-strength Damascus steel by additive manufacturing, Nature (582) (2020) 515–519.

[16] A. I. H. CommitteeASM Handbook, Volume 01 - Properties and Selection: Irons, Steels, and High-Performance Alloys, ASM International, 1990.

[17] G. Krauss, Steels - Processing, Structure, and Performance, 2nd Edition, ASM International, Materials Park, OH, 2015.

[18] W. Hearn, E. Hryha, Effect of Carbon Content on the Processability of Fe-C Alloys Produced by Laser Based Powder Bed Fusion, Frontiers in Materials 8 (2022).

[19] W. Hearn, R. Steinlechner, E. Hryha, Laser-based Powder Bed Fusion of non-weldable low-alloy steels, Powder Metall. (2021).

[20] R. Grange, C. Hribal, L. Porter, Hardness of tempered martensite in carbon and low alloy steels, Metall. Trans. A 8A (1977) 1775–1785.

[21] H. Kitaguchi, S. Lozano-Perez, M. Moody, Quantitative analysis of carbon in cementite using pulsed laser atom probe, Ultramicroscopy (147) (2014) 51–60.

[22] B. Hutchinson, J. Hagström, O. Karlsson, D. Lindell, M. Tornberg, F. Lindberg, M. Thuvander, Microstructure and hardness of as-quenched martensites (0.1-0.5%C), Acta Mater. (59) (2011) 5845–5858.

[23] L. Morsdorf, E. Emelina, B. Gault, M. Herbig, C. Tasan, Carbon redistribution in quenched and tempered lath martensite, Acta Mater. 205 (2021).

[24] M. Roumbouts, Selective Laser Sintering/Melting of Iron-Based Powders, University of Leuven, 2006.

[25] M. Chiumenti, E. Neiva, E. Salsi, M. Cervera, S. Badia, J. Moya, Z. Chen, C. Lee, C. Davies, Numerical modelling and experimental validation in Selective Laser Melting, Additive Manufacturing (18) (2017) 171–185.

[26] S. Babu, K. Hono, T. Sakurai, Atom probe field ion microscopy study of the partitioning of substitutional elements during tempering of a low-alloy steel martensite, Metall. Trans. A 25 (1994) 499–508.

[27] A. Clarke, M. Miller, R. Field, D. Coughlin, P. Gibbs, K. Clarke, D. Alexander, K. Powers, P. Papin, G. Krauss, Atomic and nanoscale chemical and structural changes in quenched and tempered 4340 steel, Acta Mater. 77 (2014) 17–27.

[28] C. Zhu, X. Xiong, A. Cerezo, R. Hardwicke, G. Krauss, G. Smith, Three-dimensional atom probe characterization of alloy element partitioning in cementite during tempering of alloy steel, Ultramicrscopy 107 (2007) 808–812.

[29] S. Babu, K. Hono, T. Sakurai, APFIM sutides on martensite tempering of Fe-C-Si-Mn low alloy steel, Appl. Surf. Sci. (67) (1993) 321–327.

[30] L. Chang, G. Smith, The Silicon Effect in the Tempering of Martensite in Steels, J. Phys. (1984) 397–401.

[31] V. Thampy, A. Fong, N. Calta, J. Wang, A. Martin, P. Depond, A. Kiss, G. Guss, Q. Xing, R. Ott, A. Van Buuren, M. Toney, J. Weker, M. Kramer, M. Matthews, C. Tassone, K. Stone, Subsurface Cooling Rates and Microstructural Response during Laser Based Metal Additive Manufacturing, Sci. Rep. (10) (2020).